Multi-timescale Affinely Adjustable Robust Reactive Power Dispatch of Distribution Networks Integrated with High Penetration of PV

Peishuai Li, *Member*, *IEEE*, Zaijun Wu, *Member*, *IEEE*, Cuo Zhang, *Member*, *IEEE*, Yan Xu, *Senior Member*, *IEEE*, Zhaoyang Dong, *Fellow*, *IEEE*, and Minqiang Hu, *Member*, *IEEE*

***Abstract*—Photovoltaic (PV) power generation has highly penetrated in distribution networks, providing clean and sustainable energy. However, its uncertain and intermittent power outputs significantly impair network operation, leading to unexpected power loss and voltage fluctuation. To address the uncertainties, this paper proposes a multi-timescale affinely adjustable robust reactive power dispatch (MTAAR-RPD) method to reduce the network power losses as well as alleviate voltage deviations and fluctuations. The MTAAR-RPD aims to coordinate on-load tap changers (OLTCs), capacitor banks (CBs), and PV inverters through a three-stage structure which covers multiple timescales of "hour-minute-second". The first stage schedules CBs and OLTCs hourly while the second stage dispatches the base reactive power outputs of PV inverter every 15 min. The third stage affinely adjusts the inverter reactive power output based on an optimized *Q-P* droop controller in real time. The three stages are coordinately optimized by an affinely adjustable robust optimization method. A solution algorithm based on a cutting plane algorithm is developed to solve the optimization problem effectively. The proposed method is verified through theoretical analysis and numerical simulations.**

***Index Terms*—Multi-timescale, photovoltaic (PV), reactive power dispatch, uncertainty, affinely adjustable robust optimization.**

Manuscript received: August 20, 2020; revised: December 17, 2020; accepted: August 13, 2021. Date of CrossCheck: August 13, 2021. Date of online publication: September 8, 2021.

This work was supported in part by the Scientific Research Foundation of Nanjing University of Science and Technology (No. AE89991/255), in part by Jiangsu Provincial Key Laboratory of Smart Grid Technology and Equipment Project, Southeast University, in part by the National Natural Science Foundation of China (No.51677025), and in part by the Science and Technology Project of State Grid Corporation (No. SGMD0000YXJS1900502).

P. Li (corresponding author) is with the School of Automation, Nanjing University of Science and Technology, Nanjing, China (e-mail: peishuai. li@njust.edu.cn).

Z. Wu and M. Hu are with Jiangsu Provincial Key Laboratory of Smart Grid Technology and Equipment, Southeast University, Nanjing, China, and they are also with the School of Electrical Engineering, Southeast University, Nanjing, China (e-mail: zjwu@seu.edu.cn; mqhu@seu.deu.cn).

C. Zhang and Z. Dong are with School of Electrical Engineering and Telecommunications, University of New South Wales, Sydney, Australia (e-mail: zhangcuo13@gmail.com; zydong@ieee.org).

Y. Xu is with School of Electrical and Electronic Engineering, Nanyang Technological University, Singapore (e-mail: xuyan@ntu.edu.sg).

DOI: 10.35833/MPCE.2020.000624

NOMENCLATURE

A. Sets and Indices

E, ij	Set and index of network branches
G	Set of sub-network number
N, i	Set and index of nodes for whole network
N^{CB}, N^{PV}	Sets of nodes connecting capacitor (CB) and photovoltaic (PV)
T, t	Set and index of operation periods
U^{PV}, U^{PD}, U^{QD}	Uncertainty sets of PV, active load, and reactive load

B. Parameters

α_i	Control parameter
$\overline{\mu}$, $\underline{\mu}$	Upper and lower bounds of uncertainty budget
$\boldsymbol{A}_t$, $\boldsymbol{B}_t$, $\boldsymbol{F}_t$, $\boldsymbol{H}_t$, $\boldsymbol{I}_t$, $\boldsymbol{K}_{l,t}$, $\boldsymbol{h}_{l,t}$	Coefficient matrices
$\boldsymbol{b}_t$, $\boldsymbol{c}$, $\boldsymbol{f}_t$, $\boldsymbol{j}_t$	Constant vectors
$N_{OLTC}^{\max}$, $N_{CB}^{\max}$	Allowed maximum switch changing times for on-load tap changer (OLTC) and CB during operation period
$\overline{P}_{i,t}^{PV}$, $\underline{P}_{i,t}^{PV}$	Upper and lower bounds of PV
$\overline{P}_{i,t}^{PD}$, $\underline{P}_{i,t}^{PD}$	Upper and lower bounds of active load
$\overline{Q}_{i,t}^{PD}$, $\underline{Q}_{i,t}^{PD}$	Upper and lower bounds of reactive load
$Q_{i,t}^{PV,\max}$, $Q_{i,t}^{PV,\min}$	The maximum and minimum limits of PV reactive power
Q_{tap}	Reactive power supply of per unit CB
$r^{\min}$	Square of the minimum tap ratio in OLTC
r_s	Difference for square of ratio between step s and step $s-1$ in OLTC
$r_{i,t}$	Disturbance parameter
r_{ij}, x_{ij}	Resistance and reactance of branch ij
$S_{i,t}^{PV}$	Capacity of PV at node i during period t
$T_{OLTC}^{\max}$, $T_{CB}^{\max}$	The maximun taps of OLTC and CB
$V_{i,t}^{\max}$, $V_{i,t}^{\min}$	Upper and lower bounds of allowed voltage
w	Droop control gain

C. Variables

$\Delta\boldsymbol{P}$, $\Delta\boldsymbol{Q}$	Active and reactive power variations
$\delta_{i,t}^{OLTC,IN}$, $\delta_{i,t}^{OLTC,DE}$	Auxiliary binary variables of OLTC
$\delta_{i,t}^{CB,IN}$, $\delta_{i,t}^{CB,DE}$	Auxiliary binary variables of CB
$\sigma_{s,t}^{OLTC}$, $\sigma_{i,s,t}^{CB}$	Dummy binary variables of OLTC and CB
$\boldsymbol{J}_0$	Jacobian matrix
$L_{i,t}$	Sensitivity of node voltage magnitude to reactive power injection
$P_{i,t}^{PV}$, $P_{i,t}^{PD}$	Actual active power of PV and active load
$Q_{i,t}^{PV}$, $Q_{i,t}^{CB}$, $Q_{i,t}^{QD}$	Reactive power of PV, CB, and reactive load
$Q_{i,t}^{PV,base}$	Reactive power base setpoint of PV
$P_{i,t}^{PV,f}$	Forecasted value of mean active power of PV
$P_{ij,t}$, $Q_{ij,t}$	Active and reactive power flow of branches
$T_{i,t}^{OLTC}$, $T_{i,t}^{CB}$	Taps of OLTC and CB
$\boldsymbol{u}_t$	Uncertain variables
$\boldsymbol{V}_0$	Bus voltage vector
$v_{base,t}$	Square of voltage for OLTC at primary side
$V_{i,t}$, $I_{ij,t}$	Node voltage magnitude and current
$V_{i,t}^{PV}$	Node voltage magnitude of bus with PV systems
$v_{i,t}$, $l_{ij,t}$	Square of node voltage magnitude and current
$\boldsymbol{x}_t$	The first-stage decision variables
$\boldsymbol{y}_t$	The second-stage decision variables

I. Introduction

THE high penetration of photovoltaics (PVs) brings significant challenges to distribution network operation due to its high uncertainty and intermittency. Regarded as important in distribution network operation, reactive power dispatch (RPD) is effective in regulating bus voltages and reducing network power losses [1]. In the RPD, on-load tap changers (OLTCs) are scheduled to regulate bus voltages while capacitor banks (CBs) and inverters of PVs are scheduled for var compensation [2]. As traditional discrete devices, the OLTCs and CBs act slowly so that these devices are scheduled over long periods such as several hours. The PV inverters are power electronics equipment that can provide continuous var compensation in RPD at a real-time-level response speed. Thus, PV inverters are suggested to be employed for real-time dispatch and control in RPD methods by IEEE 1547 working group [3].

The current RPD methods can be classified into decentralized, centralized, and hierarchical architectures [4]. In decentralized RPD, the RPD devices are controlled locally and do not need global information communication. In [5], an incremental voltage control algorithm which adjusts the reactive power gradually is designed for local voltage control. A local volt/var setting which regulates the voltage utilizing PV inverters is proposed in [6]. In [7], the purely local control architectures which take voltage, power flow, and both as inputs are discussed. In [8], a local RPD method which regulates the reactive power based on locally available information is proposed to correct the voltage deviation. The decentralized RPD is always easy and simple to implement while it needs a small amount of communication, computation, or storage resources. However, it is hard to achieve globally optimal control by decentralized RPD, stemming from its shortage in the global observation of the whole network information.

Regarded as a static optimization approach, the centralized RPD schedules OLTCs, CBs, and PV inverters coordinately to achieve control objectives from the system-wide perspective. Reference [9] analyzes the ability of inverters to provide reactive power support. In [10], a centralized reactive power compensation system optimized by minimizing the expected total cost is designed to regulate voltage, improve power factor, and reduce power losses. Reference [11] proposes a multi-objective RPD model with a switch law between optimization objectives to reduce power losses and improve power quality simultaneously. From the system-wide perspective, the centralized RPD achieves global optimality by coordinating the controllable devices. However, due to slow response speeds, it is inflexible to adjust control decisions to gusty variations of network operation status, e.g., unexpected sharp variations of PV power generation.

Considering the advantages and drawbacks of the decentralized and centralized methods, the hierarchical RPD which applies the central optimization and the local control has been developed recently. In [12], a hybrid RPD control method containing two control loops is proposed. The optimal decisions of OLTC, CBs, and static var compensators (SVCs) are determined in the coordinated control loop firstly, while the CBs and SVCs become self-controlled in the uncoordinated control loop if large variations of PV power outputs occur. In [13], a hierarchical RPD method which achieves the optimal objectives through a system-wide voltage controller in an upper layer and regulates voltage locally to trace controller setpoints at a lower layer is proposed. Reference [14] proposes a distributed hierarchical RPD method, which controls the OLTC and distributed generators employing different agents. However, in these works, the local real-time operating conditions are not considered in optimal decision making at the centralized level.

It is worth noting that the stochastic nature and uncertainties of PV power generation and loads impact the control effectiveness seriously. Conventionally, stochastic programming (SP) methods are utilized to address the uncertainties. SP is implemented based on probability distribution of uncertainties, thus [15] utilizes Beta distribution and normal distribution to describe stochastic variations of renewable energy sources and loads, respectively. Reference [16] reviews the present optimal RPD methods and proposes a stochastic model considering a voltage stability index under uncertain renewable power generation and loads. In [17], the PV inverters are managed to provide optimal reactive power compensation by a stochastic scheme, which is constructed based on the Lagrange multipliers of a second-order cone programming. Although SP has a complete theoretical architecture, its applications are limited in practice, since accurate probability distribution of uncertainties is hard to be obtained. In addition, sampled scenarios for SP problems may not cover all possible uncertainty realizations, then operating risks are left and constraint violations may still occur.

Different from SP, robust optimization (RO) methods model uncertainties by lower and upper bounds without any probability distribution information. Besides, RO obtains optimal solutions in the worst case of uncertainty realization within the bounds. In [18], a robust centralized optimal dispatch approach for PV inverter is proposed. In this approach, several PV inverters with much influence on node voltage are selected and controlled to regulate bus voltages. Reference [19] coordinately optimizes schedules of OLTC, CB, PV inverter, and distributed storage system based on the two-stage RO. An adaptive robust RPD method is proposed in [20] to reduce power losses. Compared with SP, RO can ensure operating constraints to be satisfied when uncertainties are within the predefined lower and upper bounds. Thus, due to its high solution robustness against uncertainties, RO is suggested and widely applied in the RPD methods considering uncertainties.

However, in [15]-[20], the real-time local control is not considered or discussed. In [21], the two-stage RO is utilized to schedule the OLTCs, CBs, and PV inverters in two central control stages, while the local *Q-V* droop control is employed to control PV inverters in real time. The *Q-V* control is effective in regulating voltage locally but weak in reducing power losses from the system-wide perspective. Besides, the *Q-V* control may lead to output vibrations during the system convergence procedure.

Considering the above issues are unsolved in the literature, this paper proposes a multi-timescale affinely adjustable robust RPD (MTAAR-RPD) method to coordinately operate OLTC, CBs, and PV inverters covering the whole timescale, i.e., hour, minute, and second. Scheduling OLTC, CBs, and dispatching PV inverter are coordinated through the centralized adaptive RO (ARO) while the real-time PV inverter control with a linear *Q-P* control strategy is fully considered via an affinely ARO (AARO).

Compared with the existing research, the major contributions of this paper can be summarized as follows.

1) The central and local RPD methods are coordinated in a multi-timescale "hour-minute-second" framework, in which the influences of uncertainty are fully considered.

2) A linear *Q-P* real-time control strategy regulating the inverter reactive power output according to its real-time active power output is proposed and optimized in the centralized optimization to reduce power losses.

3) The multi-timescale RPD method is optimized by an AARO method which is solved by a cut plane algorithm so that the uncertainty impacts are addressed.

II. Multi-timescale RPD Structure

The MTAAR-RPD is a coordinated control strategy which covers the "hour-minute-second" multiple timescales, fully coordinating central and local control under uncertainties. Technically, MTAAR-RPD aims to schedule and control multiple RPD devices at the corresponding timescales to reduce power losses and maintain bus voltages within an allowed range considering uncertain PV power generation and loads. The whole structure of MTAAR-RPD is shown in Fig. 1.

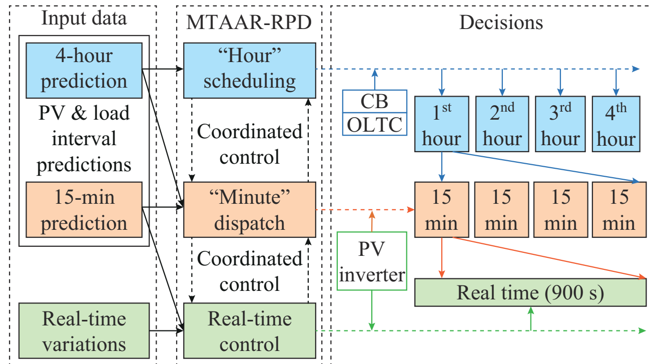

Fig. 1. Structure of MTAAR-RPD.

A. "*Hour*" *Scheduling of OLTC and CBs*

In the "hour" scheduling stage, the OLTC and CBs are scheduled optimally. To address the uncertainties, an interval prediction technique [22] is employed to provide predicted intervals. Then, based on these predicted intervals of PV active power outputs and loads over a prescribed horizon, e.g., 4 hours in this paper, the taps of an OLTC and CBs are optimized to minimize network power losses. Moreover, a rolling horizon strategy is employed to address prediction errors in the short-term future. In this strategy, only the decisions in the first hour are adopted and the decisions in the next hours will be renewed in this 4-hour horizon. The maximal switching time limitation of discrete devices over the whole scheduling horizon and the sufficient reserve capacity for the following periods are fully considered in the rolling horizon based optimization.

With consideration of the uncertainties, the "hour" scheduling and "minute" dispatch are optimized through an ARO model [21], which considers the 15-min base reactive power output of PV inverter in the "hour" scheduling of OLTC and CBs. As ARO optimizes the control decisions based on the worst case of uncertainty realization, the RPD in "hour" and "minute" timescales can be robustly coordinated. It should be noted that only the decisions of the OLTC and CBs are employed in the first hour, while PV inverter reactive power outputs will be reoptimized to be implemented in the "minute" dispatch stage.

B. "*Minute*" *Dispatch of PV Inverter*

Within each hour, the base reactive power outputs of PV inverter are scheduled to further reduce network power losses in a 15-min horizon. A 15-min-ahead interval prediction is employed and provides forecasted PV power generation and loads. Then, based on the prediction data, the optimal dispatch decisions are obtained through solving an accordingly formulated AARO model, which is introduced in Section IV.

The "minute" dispatch and "second" control are modeled in the AARO model where the "minute" dispatch decisions of PV inverter will be the reference setpoint of the "second" real-time local control. It is worth noting that the "second" real-time local control under the PV power generation fluctuations is fully considered in the "minute" inverter dispatch optimization. Thus, the RPD in these two timescales are coordinately optimized.

C. "*Second*" *Control of PV Inverter*

Within the 15-min horizon, a local *Q-P* control method is applied to reduce voltage fluctuations and power losses in real time. By utilizing a 15-min-ahead interval prediction of PV power generation, the parameters of *Q-P* control are optimized via the AARO. Then, with the optimized parameters, the inverter reactive power output is controlled according to its actual active power generation in real time. In the next 15 min, the control parameters will be updated based on the reoptimized 15-min inverter dispatch decisions.

III. Mathematical Formulation

A. *Mathematical Formulation of Q-P Control*

Reference [23] utilizes the *Q-V* droop control to regulate voltage according to the real-time voltage variations. The *Q-V* control model and its corresponding characteristic is shown as:

$$Q_{i,t}^{PV}=\begin{cases}Q_{i,t}^{PV,base}+wL_{i,t}(V_{i,t}^{\min}-V_{i,t}^{PV}) & V_{i,t}^{PV}<V_{i,t}^{\min}\\ Q_{i,t}^{PV,base} & V_{i,t}^{\min}\le V_{i,t}^{PV}\le V_{i,t}^{\max}\\ Q_{i,t}^{PV,base}+wL_{i,t}(V_{i,t}^{\max}-V_{i,t}^{PV}) & V_{i,t}^{PV}>V_{i,t}^{\max}\end{cases}\quad(1)$$

where $Q_{i,t}^{PV,\min}\le Q_{i,t}^{PV}\le Q_{i,t}^{PV,\max}$.

As shown in Fig. 2, in the *Q-V* control, the inverter reactive power is kept as $Q_{i,t}^{PV,base}$ when the voltage is within the allowed operating range $[V_{i,t}^{\min},V_{i,t}^{\max}]$. Once the voltage is beyond the allowed range, the real-time reactive power compensation is implemented through the *Q-V* droop control function. Apparently, it exists a dead band in *Q-V* control, which results in low utilization efficiency of the inverter reactive power capacity. Moreover, only the local information is utilized in this *Q-V* control, thus it is hard to operate the network optimally.

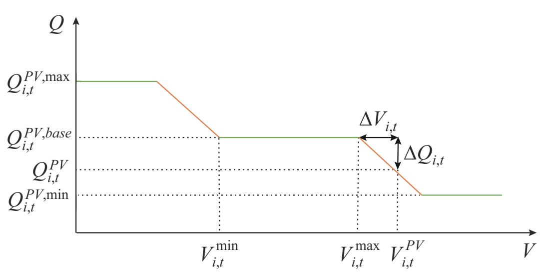

Fig. 2. Control characteristics of *Q-V* droop control.

Through fully utilizing the reactive power capacity of PV inverter and optimizing the local control in global perspective, a more effective real-time control strategy as *Q-P* control is proposed. In the proposed *Q-P* control, the reactive power of PV inverter is controlled through a linear function according to the real-time active power output. The control characteristics are illustrated in Fig. 3 and the real-time reactive power output of the i^{th} PV inverter $Q_{i,t}^{PV}$ is controlled as:

$$Q_{i,t}^{PV}=Q_{i,t}^{PV,base}+(\Delta Q_{i,t}/\Delta P_{i,t})(P_{i,t}^{PV}-P_{i,t}^{PV,f})\quad(2)$$

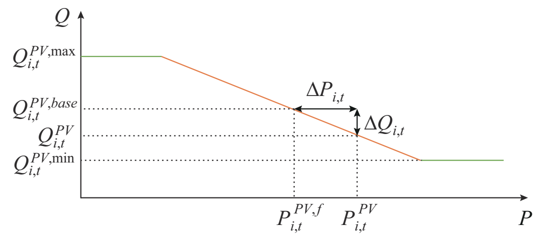

Fig. 3. Control characteristics of *Q-P* droop control.

It can be observed that the *Q-P* droop control supports more flexible reactive power control and makes more efficient utilization of the inverter capacity. Besides, as the *Q-V* control usually needs several iterations to determine the PV reactive power output based on node voltage, the vibrations may occur. By contrast, as the *Q-P* control function is linear and related to active power generation, it makes the deterministic control decision directly, therefore the vibration is avoided.

B. *Mathematical Formulation of MTAAR-RPD*

The MTAAR-RPD provides "hour" decisions for OLTC and CBs and "minute-second" decisions for PV inverter, respectively. Based on the coordinated coupling of these three controlling timescales, the mathematical model of MTAAR-RPD is shown as:

$$\min_{T_t^{OLTC},T_t^{CB},Q^{PV}}\sum_{t\in T}\sum_{ij\in E}l_{ij,t}r_{ij}\quad(3)$$

s.t.

$$\sum_{jk\in E}P_{jk,t}-\sum_{ij\in E}(P_{ij,t}-r_{ij}l_{ij,t})=P_{j,t}^{PV}-P_{j,t}^{PD}\quad\forall t\quad(4)$$

$$\sum_{jk\in E}Q_{jk,t}-\sum_{ij\in E}(Q_{ij,t}-x_{ij}l_{ij,t})=Q_{j,t}^{CB}+Q_{j,t}^{PV}-Q_{j,t}^{QD}\quad\forall t\quad(5)$$

$$v_{j,t}=v_{i,t}+(r_{ij}^2+x_{ij}^2)l_{ij,t}-2(r_{ij}P_{ij,t}+x_{ij}Q_{ij,t})\quad\forall ij\in E,\forall t\quad(6)$$

$$\left\|\begin{matrix}2P_{ij,t}\\2Q_{ij,t}\\l_{ij,t}-v_{i,t}\end{matrix}\right\|_2\le l_{ij,t}+v_{i,t}\quad\forall ij\in E,\forall t\quad(7)$$

$$(V_{i,t}^{\min})^2\le v_{i,t}\le(V_{i,t}^{\max})^2\quad\forall i\in N,\forall t\quad(8)$$

$$(I_{ij,t}^{\min})^2\le l_{ij,t}\le(I_{ij,t}^{\max})^2\quad\forall ij\in E,\forall t\quad(9)$$

$$v_{1,t}=v_{base,t}\left(r^{\min}+\sum_s r_s\sigma_{s,t}^{OLTC}\right)\quad\forall t\quad(10)$$

$$\sigma_{m-1,t}^{OLTC}\ge\sigma_{m,t}^{OLTC}\quad\forall m\in[2,T_{OLTC}^{\max}],\forall t\quad(11)$$

$$\sum_s\sigma_{s,t}^{OLTC}\le T_{OLTC}^{\max}\quad\forall t\quad(12)$$

$$\sum_s\sigma_{s,t}^{OLTC}-\sum_s\sigma_{s,t-1}^{OLTC}\ge\delta_t^{OLTC,IN}-\delta_t^{OLTC,DE}T_{OLTC}^{\max}\quad\forall t\quad(13)$$

$$\sum_s\sigma_{s,t}^{OLTC}-\sum_s\sigma_{s,t-1}^{OLTC}\le\delta_t^{OLTC,IN}T_{OLTC}^{\max}-\delta_t^{OLTC,DE}\quad\forall t\quad(14)$$

$$\sum_{t\in T}(\delta_t^{OLTC,IN}+\delta_t^{OLTC,DE})\le N_{OLTC}^{\max}\quad\forall t\quad(15)$$

$$\delta_t^{OLTC,IN}+\delta_t^{OLTC,DE}\le 1 \quad \forall t \tag{16}$$

$$Q_{i,t}^{CB}=Q_{tap}\sum_s \sigma_{i,s,t}^{CB} \quad \forall i\in N^{CB},\forall t \tag{17}$$

$$\sigma_{i,m-1,t}^{CB}\ge\sigma_{i,m,t}^{CB} \quad \forall m\in[2,T_{i,CB}^{\max}],\forall i\in N^{CB},\forall t \tag{18}$$

$$\sum_s \sigma_{i,s,t}^{CB}\le T_{i,CB}^{\max} \quad \forall i\in N^{CB},\forall t \tag{19}$$

$$\sum_s \sigma_{i,s,t}^{CB}-\sum_s \sigma_{i,s,t-1}^{CB}\ge\delta_{i,t}^{CB,IN}-\delta_{i,t}^{CB,DE}T_{i,CB}^{\max} \quad \forall i\in N^{CB},\forall t \tag{20}$$

$$\sum_s \sigma_{i,s,t}^{CB}-\sum_s \sigma_{i,s,t-1}^{CB}\le\delta_{i,t}^{CB,IN}T_{i,CB}^{\max}-\delta_{i,t}^{CB,DE} \quad \forall i\in N^{CB},\forall t \tag{21}$$

$$\begin{cases}\sum_{t\in T}(\delta_{i,t}^{CB,IN}+\delta_{i,t}^{CB,DE})\le N_i^{CB,\max} & \forall i\in N^{CB},\forall t\\ \delta_{i,t}^{CB,IN}+\delta_{i,t}^{CB,DE}\le 1 & \forall i\in N^{CB},\forall t\end{cases} \tag{22}$$

$$(P_{i,t}^{PV})^2+(Q_{i,t}^{PV})^2\le(S_{i,t}^{PV})^2 \quad \forall i\in N^{PV},\forall t \tag{23}$$

The objective function is to reduce power losses in scheduling period T, shown as (3). The power flow model is illustrated by the Dist-flow constraints as (4)-(6) while (7) is the second-order cone relaxation (SOCR) constraint. Referring to [24], when the objective function is the strictly increasing function of branch current, the SOCR is exact. This SOCR constraint transfers the non-convex power flow constants into convex ones, thus it is possible to obtain the global optimal solution. Constraints (8) and (9) indicate the safe constraints of voltage and branch current, respectively.

The operation constraints of OLTC and CB are shown in (10)-(16) and (17)-(22), respectively. Equations (10) and (11) show the voltage square relationship between the primary and secondary sides of OLTC in a linear form while (17) and (18) describe the reactive power supply of CB. Equations (12) and (19) express the maximal switch limitation of OLTC and CBs, respectively. Equations (13), (14), (20), and (21) show that the tap changes of OLTC and CBs during one operation period should be constrained within the maximum limit. Equations (15), (16), and (22) show that the total tap action times of OLTC and CBs should be limited by the allowable values during the scheduling period. Constraint (23) shows the capacity constraint of PV inverters.

During the "hour" scheduling and "minute" dispatch periods, the OLTC, CBs, and PV inverters are dispatched while the decisions are considered as definite values. Thus, (3)-(23) formulate the RPD model covering "hour-minute" timescales. Based on the optimized taps of OLTC and CBs, the PV inverter is regulated dynamically in the "second" control while the decisions relate to the real-time variations following the strategy as shown in (2). As $Q_{i,t}^{PV,base}$ is obtained during the "minute" dispatch, (2)-(10), (17), and (23) formulate the coordinated "minute" and "second" RPD model. Therefore, the "hour-minute-second" RPD model are coordinated as above.

IV. Optimization Methodology Under Uncertainty

In accordance with the RPD model constructed in Section III, the ARO is utilized in the coordinated "hour" and "minute" scheduling [18] while the AARO is employed in the coordinated "minute" and "second" controlling [25]. The details are shown as follows.

A. ARO Formulation

The uncertainties of PV active power outputs and loads are modeled by uncertainty sets U^{PV}, U^{PD}, and U^{QD} shown as:

$$U^{PV}=\left\{\underline{P}_{i,t}^{PV}\le P_{i,t}^{PV}\le\overline{P}_{i,t}^{PV},\ \underline{\mu}^{PV}\le\frac{\sum_{i\in N}\sum_{t\in T}P_{i,t}^{PV}}{\sum_{i\in N}\sum_{t\in T}P_{i,t}^{PV,f}}\le\overline{\mu}^{PV}\right\} \tag{24}$$

$$U^{PD}=\left\{\underline{P}_{i,t}^{PD}\le P_{i,t}^{PD}\le\overline{P}_{i,t}^{PD},\ \underline{\mu}^{PD}\le\frac{\sum_{i\in N}\sum_{t\in T}P_{i,t}^{PD}}{\sum_{i\in N}\sum_{t\in T}P_{i,t}^{PD,f}}\le\overline{\mu}^{PD}\right\} \tag{25}$$

$$U^{QD}=\left\{\underline{Q}_{i,t}^{QD}\le Q_{i,t}^{QD}\le\overline{Q}_{i,t}^{QD},\ \underline{\mu}^{QD}\le\frac{\sum_{i\in N}\sum_{t\in T}Q_{i,t}^{QD}}{\sum_{i\in N}\sum_{t\in T}Q_{i,t}^{QD,f}}\le\overline{\mu}^{QD}\right\} \tag{26}$$

The first terms in (24)-(26) depict the varying range of uncertain issues which can be obtained through interval prediction techniques [22]. The second terms in (24)-(26) show the budget which is utilized to balance robustness with conservativeness of solutions. The detailed illustration and discussed selection on this budget can be found in [26].

For the "hour-minute" RPD model, the OLTC and CBs are regulated hourly while the PV inverters are scheduled every 15 min, thus this model is formed in a two-stage structure. With the utilization of ARO, the first-stage decision variable is the tap of OLTC and CBs, which is known as the "here-and-now" decision. The "here-and-now" decision determined before the uncertainties are realized and cannot be changed with uncertainty. As the second-stage decision variable, the PV reactive power output is optimized according to the realization of uncertainties and this decision is referred as the "wait-and-see" decision. Then, based on ARO, the "hour-minute" RPD model is rewritten in a "min-max-min" form as:

$$\min_{x_t}\max_{u_t}\min_{y_t}\sum_{t\in T}C_t(\boldsymbol{y}_t) \tag{27}$$

s.t.

$$\boldsymbol{A}_t\boldsymbol{x}_t\le\boldsymbol{b}_t \quad \forall t \tag{28}$$

$$\sum_{t\in T}\boldsymbol{B}_t\boldsymbol{x}_t\le\boldsymbol{c} \quad \forall t \tag{29}$$

$$\boldsymbol{F}_t\boldsymbol{y}_t\le\boldsymbol{f}_t \quad \forall t \tag{30}$$

$$\boldsymbol{H}_t\boldsymbol{x}_t+\boldsymbol{I}_t\boldsymbol{y}_t+\boldsymbol{J}_t\boldsymbol{u}_t=\boldsymbol{j}_t \quad \forall t \tag{31}$$

$$\left\|\boldsymbol{K}_{l,t}\boldsymbol{y}_t\right\|\le\boldsymbol{h}_{l,t}^{\mathrm{T}}\boldsymbol{y}_t \quad \forall t \tag{32}$$

$$\boldsymbol{u}_t\in U \quad \forall t \tag{33}$$

Equation (27) denotes the objective function. The action limits of OLTC and CBs (expressed as (10)-(12) and (17)-(19), respectively) are expressed by constraint (28). Constraint (29) denotes the time coupling of OLTC and CBs (expressed as (13)-(16) and (20)-(22), respectively). Constraints (8), (9), and (23) are integrated as constraint (30). Equation (31) denotes constraints (4)-(6). The SOCR constraint shown as (7) is expressed by (32) and (33) shows the uncertainty sets as (24)-(26), where $U = U^{PV} \cup U^{PD} \cup U^{QD}$.

In this "min-max-min" formulation, it minimizes power losses under the worst case in the uncertain set. The second "min" aims to optimize the second-stage dispatch decision under the worst case which is searched by the "max". Based on the second-stage dispatch decisions and the obtained worst case, the first-stage scheduling decisions are optimized by the first "min". Thus, the first and second RPD stages can be optimized coordinately and robustly.

B. AARO Formulation

With the 15-min-ahead interval prediction, the uncertain PV active power is illustrated as (24). As the strict requirement of safety in real-time operation, the regulation budget is not employed. By applying the affine mathematic, the active power output of an arbitrary PV can be obtained as:

$$P_{i,t}^{PV} = P_{i,t}^{PV,f} + \beta_{i,t} r_{i,t} \tag{34}$$

$$\beta_{i,t} = (\overline{P}_{i,t}^{PV} - \underline{P}_{i,t}^{PV})/2 \tag{35}$$

Then, with the *Q-P* control, the reactive power output is updated by the following affine function:

$$Q_{i,t}^{PV} = Q_{i,t}^{PV,base} + \alpha_{i,t} r_{i,t} \tag{36}$$

$$r_{i,t} = (P_{i,t}^{PV} - P_{i,t}^{PV,f})/\beta_{i,t} \tag{37}$$

It should be noted that (2) and (36) are equivalent while (2) shows the physical meaning and (36) is utilized to present the AARO mathematical model easily.

Accordingly, the capacity constraint is written as:

$$(P_{i,t}^{PV,f} + \beta_{i,t} r_{i,t})^2 + (Q_{i,t}^{PV,base} + \alpha_{i,t} r_{i,t})^2 \leq (S_{i,t}^{PV})^2 \tag{38}$$

The renewed capacity constraint (38) is quadratic, and it causes the AARO model to be complex and hard to solve. Then, the inner approximation [26] is designed to transfer the quadratic constraint into a group of linear constraints, as shown in Fig. 4.

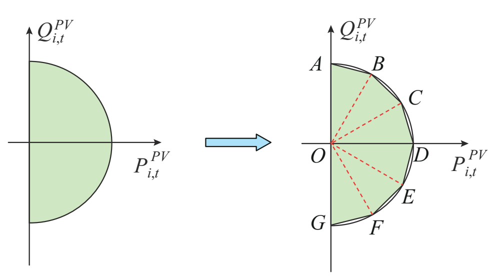

Fig. 4. Inner approximation of capacity constraint.

The original capacity constraint shown as a semi-circle is transferred into the constraint described by the area which is formed by the line segments (*A*, *B*), (*B*, *C*), (*C*, *D*), (*D*, *E*), (*E*, *F*), (*F*, *G*), and (*G*, *A*). Then, the line segment (*A*, *B*) can be shown as:

$$Q_{i,t}^{PV,base} + \alpha_{i,t} r_{i,t} - (P_{i,t}^{PV,f} + \beta_{i,t} r_{i,t} - S_{i,t}^{PV})/(\sqrt{3} - 2) \leq 0 \tag{39}$$

The other line segments (*B*, *C*), (*C*, *D*), (*D*, *E*), (*E*, *F*), (*F*, *G*), and (*G*, *A*) can be expressed in a similar way. For the inner approximation, the segments can be changed according to practical requirements. More segments are used to increase accuracy and less segments are used to speed up computation. As the PV active power variation is always small compared with the active power output, it can be concluded that if the above constraints are guaranteed under the extreme points as $r_{i,t} = 1$ and $r_{i,t} = -1$, they can be satisfied with other conditions. To simplify the expression, the above constraints are represented by $\boldsymbol{h}(Q_{i,t}^{PV,base}, \alpha_{i,t}, r_{i,t}) \leq \boldsymbol{0}$.

As the traditional voltage constraint (8) is static, it is insufficient to guarantee the safe operation with dynamic voltage variation in real time. Then, a novel AARO voltage constraint is proposed in this paper.

Based on the sensitivity equation from Newton-Raphson method, we can obtain:

$$\begin{bmatrix} \Delta \boldsymbol{P} \\ \Delta \boldsymbol{Q} \end{bmatrix} = \boldsymbol{J}_0 \begin{bmatrix} \Delta \boldsymbol{\theta} \\ \Delta \boldsymbol{V} \end{bmatrix} \tag{40}$$

$$\boldsymbol{J}_0^{-1} = \boldsymbol{S} = \begin{bmatrix} \boldsymbol{S}_P^{\theta} & \boldsymbol{S}_Q^{\theta} \\ \boldsymbol{S}_P^{V} & \boldsymbol{S}_Q^{V} \end{bmatrix} \tag{41}$$

$$\boldsymbol{V} = \boldsymbol{V}_0 + \Delta \boldsymbol{V} = \boldsymbol{V}_0 + \boldsymbol{S}_P^V \Delta \boldsymbol{P} + \boldsymbol{S}_Q^V \Delta \boldsymbol{Q} \tag{42}$$

$$\begin{cases} \Delta P_{i,t} = \beta_{i,t} r_{i,t} & \forall i \in N^{PV}, \forall t \\ \Delta Q_{i,t} = \alpha_{i,t} r_{i,t} & \forall i \in N^{PV}, \forall t \end{cases} \tag{43}$$

Then, (40)-(43) illustrate the relationship between node voltage magnitude and PV power supplies in real time. Based on this linear relationship, the constraints of node voltage can be transferred into the constraints on PV power supplies in real time.

Based on the above analysis, the AARO model is expressed as:

$$\min_{Q_t^{PV,base}, \boldsymbol{\alpha}} \max_{\boldsymbol{r}} \sum_{t \in T} \sum_{ij \in E} r_{ij} l_{ij,t} \tag{44}$$

s.t.

$$\begin{cases} \boldsymbol{h}(Q_{i,t}^{PV,base}, \alpha_{i,t}, r_{i,t}) \leq 0 \quad \forall i \in N^{PV}, \forall t \\ \boldsymbol{V}_t^{\min} \leq \boldsymbol{V}_{0,t} + \boldsymbol{S}_P^V \Delta \boldsymbol{P}_t + \boldsymbol{S}_Q^V \Delta \boldsymbol{Q}_t \leq \boldsymbol{V}_t^{\max} \quad \forall t \\ (4)\text{-}(6), (8)\text{-}(10), (17), (34)\text{-}(37), (40)\text{-}(43) \end{cases} \tag{45}$$

C. Solution Method

The ARO model which schedules OLTC and CBs is solved by applying the column and constraint generation (C&CG) algorithm and the detailed illustration of C&CG can be found in [27]. From the linear function shown in (36), the control variables to be acquired are $\boldsymbol{Q}_t^{PV,base}$ and $\boldsymbol{\alpha}$. By considering (36) and (37) together, it can be concluded that if the disturbance parameter $\boldsymbol{r}$ equals to $\boldsymbol{0}$, the PV active power is the forecasted value and the optimal reactive power $\boldsymbol{Q}_t^{PV}$ equals to $\boldsymbol{Q}_t^{PV,base}$. Thus, $\boldsymbol{Q}_t^{PV,base}$ can be obtained by solving the AARO mathematical model with $\boldsymbol{r} = \boldsymbol{0}$, which is a deterministic optimization model.

With known $\boldsymbol{Q}_t^{PV,base}$, the unknown parameters in (36) are $\boldsymbol{\alpha}$ and $\boldsymbol{r}$. The objective function of AARO in (44) is transformed to $\min_{\boldsymbol{\alpha}} \max_{\boldsymbol{r}} f(\boldsymbol{\alpha}, \boldsymbol{r})$. It is assumed that $(\boldsymbol{\alpha}^*, \boldsymbol{r}^*)$ is the optimal solution, $(\boldsymbol{\alpha}^k, \boldsymbol{r}^k)$ is one pair of arbitrary values within the feasible region of the original problem. Then, the following constraints are satisfied:

$$\min_{\boldsymbol{\alpha}^*}\max_{\boldsymbol{r}^*} f(\boldsymbol{\alpha}^*,\boldsymbol{r}^*)\geq \min_{\boldsymbol{\alpha}} f(\boldsymbol{\alpha},\boldsymbol{r}^*)\geq \min_{\boldsymbol{\alpha}} f(\boldsymbol{\alpha},\boldsymbol{r}^k) \tag{46}$$

$$\min_{\boldsymbol{\alpha}^*}\max_{\boldsymbol{r}^*} f(\boldsymbol{\alpha}^*,\boldsymbol{r}^*)\leq \max_{\boldsymbol{r}} f(\boldsymbol{\alpha}^*,\boldsymbol{r})\leq \max_{\boldsymbol{r}} f(\boldsymbol{\alpha}^k,\boldsymbol{r}) \tag{47}$$

By analyzing (46) and (47) together, the min-max problem is one saddle point problem, which is solved by a cutting plane algorithm. The detailed procedure of solution method for AARO is shown in Algorithm 1.

Algorithm 1: procedure of solution method for AARO

1: Initialize $\boldsymbol{r}^0=\boldsymbol{0}$, solve the deterministic optimization problem and obtain $\boldsymbol{Q}_t^{PV,base}$.
2: Set the iteration time $k=1$, the iteration convergence standard $\varepsilon=1\times 10^{-2}$, the upper bound $UB=+\infty$ and the lower bound $LB=-\infty$.
3: **while** $|UB-LB|>\varepsilon$ **do**
4: Set $\boldsymbol{r}=\boldsymbol{r}^{k-1}$, solve the AARO model to obtain $\boldsymbol{\alpha}^k$, then update $LB=\min_{\boldsymbol{\alpha}} f(\boldsymbol{\alpha},\boldsymbol{r}^{k-1})$.
5: Set $\boldsymbol{\alpha}=\boldsymbol{\alpha}^k$, solve the AARO model to obtain $\boldsymbol{r}^k$, then update $UB=\max_{\boldsymbol{r}} f(\boldsymbol{\alpha}^k,\boldsymbol{r})$ and $k=k+1$.
6: **end**

V. Case Studies

A. Test System

The IEEE 123-bus distribution network, whose data can be found in [2], is utilized to testify the efficiency of the proposed MTAAR-RPD approach. The OLTC, CBs, and PVs are installed while the parameters are shown in Table I. The voltage of OLTC at the primary side is set as 1.0 p.u. and the voltage regulation scope is set as [0.95, 1.05] p.u.

TABLE I
Parameters of OLTC, CBs and PVs

Type	Limit taps	Per tap/ capacity	Bus No. of placement location
OLTC	20	0.005 p.u.	1
CB	10	30 kvar	19, 50, 70, 83, 96, 118
PV		600 kVA	15, 25, 40, 51, 65, 77, 85, 95, 97, 113

The uncertainties of loads and PV power generation are illustrated as follows. As for the PV active power, the lower and upper bounds of 4-hour-ahead prediction are set as 0.7 and 1.3 of the expected value, respectively, while the bounds of uncertainty budgets are set as 0.8 and 1.2. Moreover, its 15-min-ahead predicted lower and upper bounds of the 15-min-ahead prediction are set as 0.8 and 1.2 of the expected value, respectively. In terms of loads, the predicted lower and upper bounds are set as 0.8 and 1.2 of the expected value, respectively, while the bounds of uncertainty budgets are set as 0.9 and 1.1, respectively. The multiplier factors of the uncertain issues are shown in Fig. 5 while the predicted and actual values of these issues equal to their base value times of the corresponding factors.

B. "Hour" and "Minute" Controlling Decisions

The decisions of OLTC and CBs are optimized for the 4-hour scheduling period while only decisions in the first hour are adopted. And this procedure is rolled hourly.

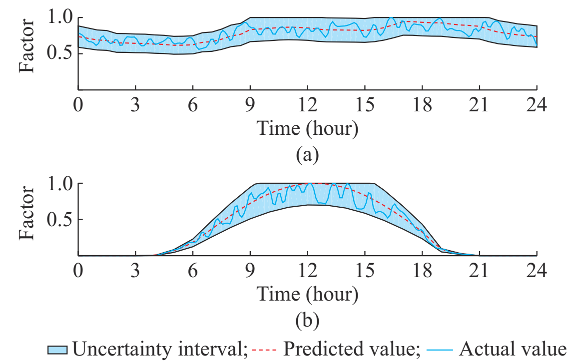

Fig. 5. Uncertain load and PV factors in 24 hours. (a) Load. (b) PV.

Based on the predicted interval of PV generation and loads, the decisions of OLTC and CBs are obtained through solving the ARO model. Figure 6 shows the tap decisions of the OLTC and CBs from 8 a.m. to 12 a.m., in other words, the decisions shown are for the 1-hour time sections starting at 08:00, 09:00, 10:00, and 11:00, respectively.

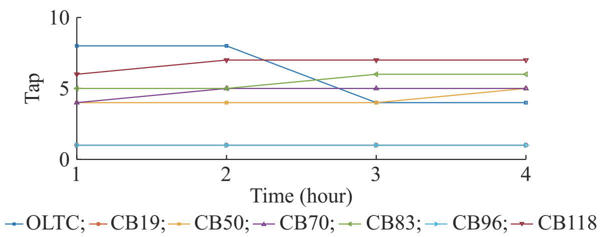

Fig. 6. Tap decisions of OLTC and CBs.

Within each hour, the "minute" controlling decisions of PV reactive power contribution are obtained by solving a deterministic optimization model based on the obtained results of OLTC and CBs. The controlling decisions of PV reactive power from 08:00 to 08:45 are shown in Fig. 7.

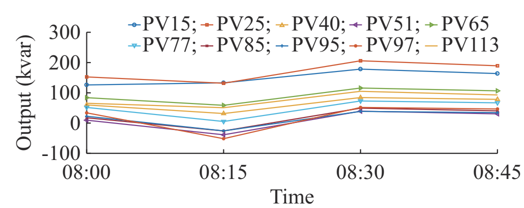

Fig. 7. Controlling decisions of PV reactive power.

It should be noted that, the decisions in Fig. 7 are obtained by solving the "minute" control model, which are not the real-time decisions of the PV reactive power outputs. In real-time operation, the PV reactive power output will be regulated by employing the "second" control proposed in this paper with the updated real-time measurements. The "hour-minute" scheduling model in the ARO form is solved in 26.7107 s, indicating the proposed method is fully compatible for practical online use.

C. Real-time Controlling Decisions

To test the performance of proposed *Q-P* control, a random scenario for period from 08:00 to 08:15 (900 s) is constructed while the real-time PV power generation factor is shown in Fig. 8. It should be noted that the PV power generation fluctuates beyond the given lower and upper bounds of uncertainty to simulate the actual scenario as the sudden cloud movement.

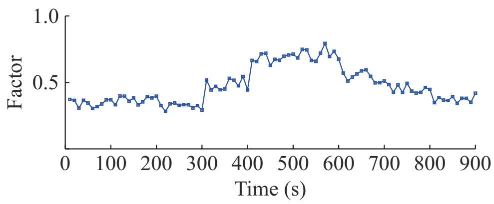

Fig. 8. PV power generation factor in 900 s.

In the *Q-P* control, the control parameters are obtained by solving the AARO model with the proposed cut plane algorithm. And the AARO model is solved in 3.5878 s, which meets the requirement of practical online use. During the time period from 08:00 to 08:15, the controlled reactive power outputs of PV inverters are shown in Fig. 9. Correspondingly, the voltage magnitude of the network at $t=410$ s employing *Q-P* control is shown in Fig. 10.

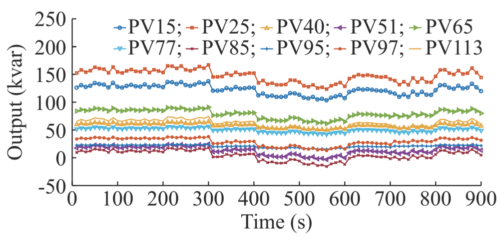

Fig. 9. Real-time reactive power outputs of PV inverters with *Q-P* control.

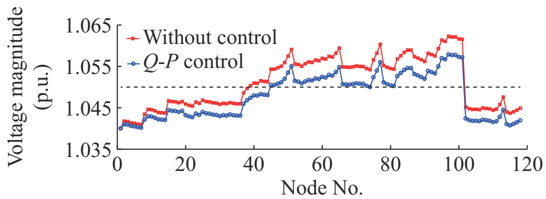

Fig. 10. Voltage magnitude of network at $t=410$ s.

To test the proposed *Q-P* strategy, the comparison between *Q-P* control and *Q-V* control on a 900-second scenario is conducted as follows. The parameters of *Q-V* control strategy are not optimized but set as a traditional model, and the details of *Q-V* control can be found in [5]. The convergence procedures of *Q-V* control and *Q-P* control at four locations are shown in Fig. 11. The comparison on voltage regulation is shown in Fig. 12.

As shown in Fig. 11, the proposed *Q-P* control achieves flat control results while the *Q-V* control leads to vibration. This is because the *Q-P* control is based on active power, thus the decision on PV reactive power output can be obtained directly based on the measurement of real-time active power output in (36).

However, the *Q-V* control is voltage-based and voltage can only be obtained via power flow calculation.

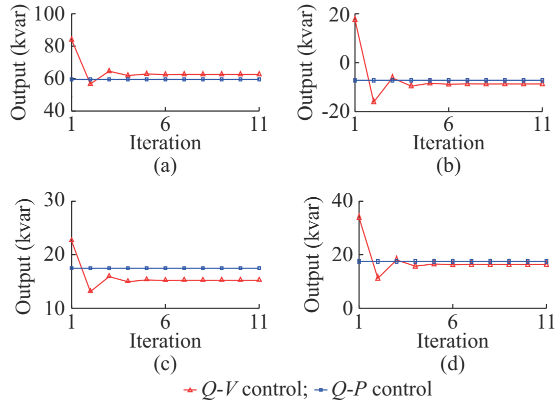

Fig. 11. Convergence procedures of *Q-V* control and *Q-P* control. (a) Location 1. (b) Location 2. (c) Location 3. (d) Location 4.

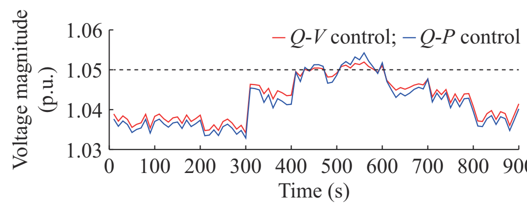

Fig. 12. Voltage magnitude of node 44 under *Q-V* and *Q-P* controls.

Moreover, the relationship between the bus voltage and reactive power injection is non-linear, and it usually needs iterations for converging the reactive power output and the voltage operating point on the *Q-V* droop curve. Thus, *Q-V* control needs time for making decisions when power flow changes, which leads to slight vibrations.

From Fig. 12, the *Q-V* control behaves slightly better in alleviating voltage fluctuations when voltage is over 1.05 p.u.. However, under the condition that bus voltages are within the allowed regulation scope, *Q-P* control provides a lower voltage level, for it can better track PV power fluctuations with fully-optimized control parameters.

Besides, the average power losses of *Q-V* control and *Q-P* control are 17.702 kW and 16.401 kW, respectively. It can be observed that *Q-P* control significantly reduces 7.35% power losses more than *Q-V* control from 08: 00 to 08: 15. Thus, *Q-P* control achieves less power loss, and more economic benefits than *Q-V* control.

These two strategies are applicable under different conditions. If the distribution network operates in the normal voltage level, the *Q-P* control is more effective. On the other hand, if the distribution network operates under the risk of overvoltage, the *Q-V* control is more applicable.

D. 24-hour Scenario

As shown in Fig. 6, the 24-hour scenario is constructed to testify the effectiveness of the proposed MTAAR-RPD in a whole day. The uncertain bounds of 4-hour-ahead prediction are utilized in optimizing the “hour-minute” dispatch with rolling horizon while uncertain bounds of 15-min-ahead prediction and actual value of PV power generation are employed in optimizing the “minute-second” control. Then, the decisions of OLTC and CBs are shown in Fig. 13 while reactive power outputs of PVs are shown in Fig. 14.

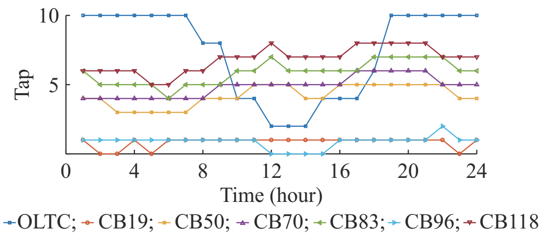

Fig. 13. Decisions of OLTC and CBs in 24 hours.

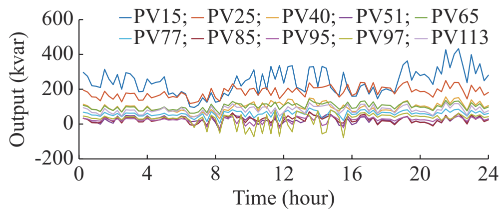

Fig. 14. Reactive power outputs of PVs in 24 hours.

As shown in Fig. 13, the OLTC acts with low tap to bring down the voltage level during the hours with high PV active power supply, i.e., 10:00-17:00, while it acts with high tap during the hours with low PV active power supply, i.e., 00:00-07:00 and 19:00-24:00. During the hours with high demand and low PV active power supply, CBs provide high reactive power output to maintain the voltage level. It can be observed from Fig. 14 that PVs provide less or even absorb reactive power from the distribution network with the increase of actual active power supply of PVs, i.e., 11:45-12:00. Moreover, reactive power decisions of PVs fluctuate in large range when their active power supplies fluctuate heavily, i.e., 10:00-14:00.

Figure 15 shows the power losses of the test system with and without RPD in 24 hours. The average power loss is 79.0729 kW without RPD while the loss is significantly reduced to 53.9479 kW by employing the proposed MTAAR-RPD. Thus, the reduction rate is regarded as 31.77%.

On the other hand, as shown in Fig. 16, by employing the MTAAR-RPD, the hourly voltage profiles for all the buses are improved to avoid bus voltage violations and concentrate much with small deviations.

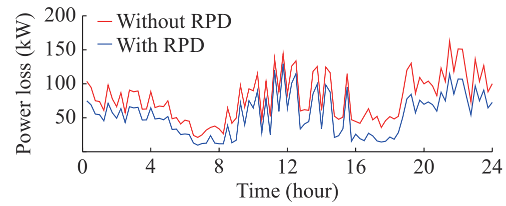

Fig. 15. Power losses of test system with and without RPD.

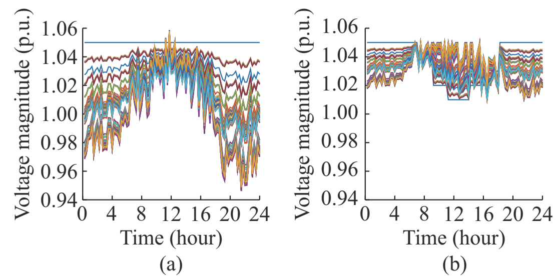

Fig. 16. Voltage profiles for all buses in IEEE 123-bus system. (a) Without RPD. (b) With MTAAR-RPD.

E. Robustness Verification of MTAAR-RPD

To verify the robustness of the proposed method, the comparison of MTAAR-RPD with the multi-timescale deterministic RPD (MTD-RPD) is implemented with the Monte Carlo simulation (MCS). The dispatch is performed every 15 min, thus there are 96 short periods in 24 hours. In MCS, 300 random scenarios with norm distribution, whose standard variations for PV and load are 0.1 and 0.05, respectively, are generated during each short period. Thus, there are 28800 scenarios in total.

As in the MTD-RPD, the scheduling decisions are acquired based on the point prediction of loads and PV active power, neglecting the uncertainties. By employing these two methods in the 28800 scenarios, respectively, the corresponding dispatch decisions are acquired firstly. Then, the power losses and voltage deviation of utilizing MTD-RPD and MTAAR-RPD are obtained and the results are shown in Table II.

TABLE II
COMPARISON RESULTS BETWEEN MTD-RPD AND MTAAR-RPD

Method	Number of infeasible cases	Actual maximal loss (kW)	Actual average loss (kW)	Voltage absolute deviation (p.u.)	Total OLTC tap changes	Total CB switches	Average PV reactive power (kvar)
MTD-RPD	4632	161.151	56.195	0.0185	6	31	95.583
MTAAR-RPD	0	149.135	55.857	0.0169	5	34	91.612

From Table II, it can be observed that the total OLTC tap changes are 5 and the total CB tap switches are 34 when the MTAAR-RPD is utilized. Then, both of these changes meet the daily maximal limitations 6 and 48, respectively. Moreover, the average PV reactive power output of MTAAR-RPD is 91.612 kvar which is less than that of MTD-RPD, showing better control performance. There are 4632 infeasible cases with MTD-RPD while MTAAR-RPD provides valid scheduling decisions for all the 28800 cases. It is shown that the MTD-RPD which is the deterministic optimization method is not applicable with uncertain loads and PV active power. Moreover, the MTAAR-RPD provides less power losses and voltage deviation, which shows its effectiveness in power losses reduction and voltage regulation. In conclusion, the MTAAR-RPD provides robustly and efficiently optimized decisions in reducing power losses and regulating voltage under uncertainties.

VI. Conclusion

This paper proposes an MTAAR-RPD method to robustly reduce power losses and alleviate voltage fluctuations in a three-stage structure covering "hour-minute-second" multiple timescales. The OLTC and CBs are scheduled hourly in the first stage while reactive power of PV inverter is scheduled every 15 minutes in the second stage. The third stage controls PV reactive power output through an optimized *Q*-*P* control in real time. To address the uncertainties, the coordinated "hour-minute" control is formulated in an ARO model while the coordinated "minute-second" *Q*-*P* control is formulated in an AARO model. The ARO model is solved by the C&CG algorithm while the AARO model is solved by a proposed cutting plane algorithm.

In the case study, the proposed MTAAR-RPD method is executed on the IEEE 123-bus system. The simulation results verify that the three stages are effectively coordinated among "hour-minute-second" multiple timescales to achieve optimal operating results. Compared with the existing methods, the proposed method can achieve significantly less power losses and better voltage profiles. Moreover, the solutions are fully robust against any uncertainty realization.

References

[1] Rabih A. Jabr, "Power flow based volt/var optimization under uncertainty," *Journal of Modern Power Systems and Clean Energy*, vol. 9, no. 5, pp. 1000-1006, Sept. 2021.

[2] P. Li, C. Zhang, Z. Wu *et al.*, "Distributed adaptive robust voltage/var control with network partition in active distribution networks," *IEEE Transactions on Smart Grid*, vol. 11, no. 3, pp. 2245-2256, May 2020.

[3] *IEEE Standard Conformance Test Procedures for Equipment Interconnecting Distributed Energy Resources with Electric Power Systems and Associated Interfaces*, IEEE Standard 1547.1-2020, pp. 1-282, 2020.

[4] Q. Li, Y. Zhang, T. Ji *et al.*, "Volt/var control for power grids with connections of large-scale wind farms: a review," *IEEE Access*, vol. 6, pp. 26675-26692, May 2018.

[5] M. Farivar, X. Zho, and L. Che, "Local voltage control in distribution systems: an incremental control algorithm," in *Proceedings of 2015 IEEE International Conference on Smart Grid Communications (SmartGridComm)*, Miami, USA, Nov. 2015, pp. 732-737.

[6] M. Rylander, H. Li, J. Smith *et al.*, "Default volt-var inverter settings to improve distribution system performance," in *Proceedings of 2016 IEEE Power and Energy Society General Meeting (PESGM)*, Boston, USA, Jul. 2016, pp. 1-5.

[7] K. Turitsyn, P. Sulc, S. Backhaus *et al.*, "Options for control of reactive power by distributed photovoltaic generators," *Proceedings of the IEEE*, vol. 99, no. 6, pp. 1063-1073, Jun. 2011.

[8] B. A. Robbins, C. N. Hadjicostis, and A. D. Domínguez-García, "A two-stage distributed architecture for voltage control in power distribution systems," *IEEE Transactions on Power Systems*, vol. 28, no. 2, pp. 1470-1482, May 2013.

[9] R. Majumder, "Aspect of voltage stability and reactive power support in active distribution," *IET Generation, Transmission & Distribution*, vol. 8, no. 3, pp. 442-450, Mar. 2014.

[10] S. X. Chen, Y. S. F. Eddy, H. B. Gooi *et al.*, "A centralized reactive power compensation system for LV distribution networks," *IEEE Transactions on Power Systems*, vol. 30, no. 1, pp. 274-284, Jan. 2015.

[11] H. Yeh, D. F. Gayme, and S. H. Low, "Adaptive var control for distribution circuits with photovoltaic generators," *IEEE Transactions on Power Systems*, vol. 27, no. 3, pp. 1656-1663, Aug. 2012.

[12] Z. Wang, H. Chen, J. Wang *et al.*, "Inverter-less hybrid voltage/var control for distribution circuits with photovoltaic generators," *IEEE Transactions on Smart Grid*, vol. 5, no. 6, pp. 2718-2728, Nov. 2014.

[13] Q. Guo, H. Sun, B. Wang *et al.*, "Hierarchical automatic voltage control for integration of large-scale wind power: design and implementation," *Electric Power Systems Research*, vol. 120, pp. 234-241, Mar. 2015.

[14] H. Wu, C. Huang, M. Ding *et al.*, "Distributed cooperative voltage control based on curve-fitting in active distribution networks," *Journal of Modern Power Systems and Clean Energy*, vol. 5, no. 5, pp. 777-786, Sept. 2017.

[15] Y. Xu, Z. Y. Dong, R. Zhang *et al.*, "Multi-timescale coordinated voltage/var control of high renewable-penetrated distribution systems," *IEEE Transactions on Power Systems*, vol. 32, no. 6, pp. 4398-4408, Nov. 2017.

[16] S. M. Mohseni-Bonab and A. Rabiee, "Optimal reactive power dispatch: a review, and a new stochastic voltage stability constrained multi-objective model at the presence of uncertain wind power generation," *IET Generation, Transmission & Distribution*, vol. 11, no. 4, pp. 815-829, Mar. 2017.

[17] V. Kekatos, G. Wang, A. J. Conejo *et al.*, "Stochastic reactive power management in microgrids with renewables," *IEEE Transactions on Power Systems*, vol. 30, no. 6, pp. 3386-3395, Nov. 2015.

[18] T. Ding, C. Li, Y. Yang *et al.*, "A two-stage robust optimization for centralized-optimal dispatch of photovoltaic inverters in active distribution networks," *IEEE Transactions on Sustainable Energy*, vol. 8, no. 2, pp. 744-754, Apr. 2017.

[19] H. Gao, J. Liu, and L. Wang, "Robust coordinated optimization of active and reactive power in active distribution systems," *IEEE Transactions on Smart Grid*, vol. 9, no. 5, pp. 4436-4447, Sept. 2018.

[20] P. Li, Z. Wu, Y. Wang *et al.*, "Adaptive robust optimal reactive power dispatch in unbalanced distribution networks with high penetration of distributed generation," *IET Generation, Transmission & Distribution*, vol. 12, no. 6, pp. 1382-1389, Mar. 2018.

[21] C. Zhang, Y. Xu, and Z. Dong *et al.*, "Three-stage robust inverter-based voltage/var control for distribution networks with high-level PV," *IEEE Transactions on Smart Grid*, vol. 10, no. 1, pp. 782-793, Jan. 2019.

[22] C. Wan, Z. Xu, P. Pinson *et al.*, "Probabilistic forecasting of wind power generation using extreme learning machine," *IEEE Transactions on Power Systems*, vol. 29, no. 3, pp. 1033-1044, May 2014.

[23] C. Zhang and Y. Xu, "Hierarchically-coordinated voltage/var control of distribution networks using PV inverters," *IEEE Transactions on Smart Grid*, vol. 11, no. 4, pp. 2942-2953, Jul. 2020.

[24] M. Farivar and S. H. Low, "Branch flow model: relaxations and convexification—part I," *IEEE Transactions on Power Systems*, vol. 28, no. 3, pp. 2554-2564, Aug. 2013.

[25] D. Bertsimas, B. B. David, and C. Constantine. "Theory and applications of robust optimization," *Society for Industrial and Applied Mathematics Review*, vol. 53, no. 3, pp. 464-501, Aug. 2011.

[26] C. Zhang, Y. Xu, and Z. Y. Dong, "Robustly coordinated operation of a multi-energy micro-grid in grid-connected and islanded modes under uncertainties," *IEEE Transactions on Sustainable Energy*, vol. 11, no. 2, pp. 640-651, Apr. 2020.

[27] B. Zeng and L. Zhao, "Solving two-stage robust optimization problems using a column-and-constraint generation method," *Operations Research Letters*, vol. 41, no. 5, pp. 457-461, Sept. 2013.

Peishuai Li received the B.E. degree in automation engineering from Qingdao University, Qingdao, China, in 2010, the M.E. degree in electrical power system and its automation form Shandong University, Jinan, China, in 2013, and the Ph. D. degree in electrical engineering from Southeast University, Nanjing, China, in 2019. From October 2017 to October 2018, he was a Visiting Ph. D. student in University of New South Wales, Sydney, Australia. He is currently a Lecturer with Nanjing University of Science and Technology, Nanjing, China. His research interests include power system operation, active distribution networks, microgrid, and application of optimization theory in these areas.

Zaijun Wu received the B.Eng. degree in power system and its automation from Hefei University of Technology, Hefei, China, in 1996, and the Ph.D. degree in electrical engineering from Southeast University, Nanjing, China, in 2004. He was a Visiting Scholar in the Ohio State University, Columbus, USA, from 2012 to 2013. He is currently a Professor in the School of Electrical Engineering, Southeast University. His research interests include substation automation, microgrid, and active distribution networks.

Cuo Zhang received the B. E. (Hons.) degree in electrical (power) engineering from The University of Sydney, Sydney, Australia, in 2014, and the Ph. D. degree in electrical engineering from the University of New South Wales, Sydney, Australia, in 2018. He is now the Research Associate with the University of New South Wales. His research interests include pow-

er system planning and operation, voltage stability and control, microgrids, multi-energy systems, and applications of optimization theory in these areas.

Yan Xu received the B.E. and M.E degrees from South China University of Technology, Guangzhou, China, in 2008 and 2011, respectively, and the Ph.D. degree from The University of Newcastle, Newcastle, Australia, in 2013. He conducted postdoctoral research with the University of Sydney Postdoctoral Fellowship, Sydney, Australia, and then joined Nanyang Technological University (NTU) with The Nanyang Assistant Professorship, Singapore. He is now an Associate Professor at School of Electrical and Electronic Engineering and a Cluster Director at Energy Research Institute @ NTU (ERI@N). He is also serving as the Chairman for IEEE Power & Energy Society Singapore Chapter. His research interests include power system stability and control, microgrid, and data-analytics for smart grid applications.

Zhaoyang Dong received the Ph.D. degree from The University of Sydney, Sydney, Australia, in 1999. He is currently the SHARP Professor with the University of New South Wales, Sydney, Australia. He was an Ausgrid Chair, Director of the Ausgrid Centre for Intelligent Electricity Networks, the University of Newcastle, Newcastle, Australia, and Head of School of Electrical and Information Engineering, The University of Sydney. He also worked as manager for system planning with Transend Networks (now TAS-Networks), Australia. His research interests include smart grid, power system planning, power system security, renewable energy systems, electricity market, and computational intelligence and its application in power engineering.

Minqiang Hu received the Ph.D. degree in electrical engineering from Huazhong University of Science and Technology, Wuhan, China, in 1990. He is currently a full Professor in the School of Electrical Engineering, Southeast University, Nanjing, China. His research interests include electric machine modeling and simulation, and renewable energy.